How van der Waals interactions determine the unique properties of water

Tobias Morawietz[a,1,2], Andreas Singraber[b], Christoph Dellago[b], and Jörg Behler[a,1]

[a]Lehrstuhl für Theoretische Chemie, Ruhr-Universität Bochum, D-44780 Bochum, Germany; and [b]Faculty of Physics, University of Vienna, A-1090 Vienna, Austria

Edited by Christopher J. Mundy, Pacific Northwest National Laboratory, Richland, WA, and accepted by Editorial Board Member John D. Weeks June 1, 2016 (received for review February 19, 2016)

Whereas the interactions between water molecules are dominated by strongly directional hydrogen bonds (HBs), it was recently proposed that relatively weak, isotropic van der Waals (vdW) forces are essential for understanding the properties of liquid water and ice. This insight was derived from ab initio computer simulations, which provide an unbiased description of water at the atomic level and yield information on the underlying molecular forces. However, the high computational cost of such simulations prevents the systematic investigation of the influence of vdW forces on the thermodynamic anomalies of water. Here, we develop efficient ab initio-quality neural network potentials and use them to demonstrate that vdW interactions are crucial for the formation of water's density maximum and its negative volume of melting. Both phenomena can be explained by the flexibility of the HB network, which is the result of a delicate balance of weak vdW forces, causing, e.g., a pronounced expansion of the second solvation shell upon cooling that induces the density maximum.

water structure | van der Waals interactions | neural network potentials | ab initio liquid water | density-functional theory

Water is an exceptional liquid exhibiting several anomalies, of which the density maximum at 4 °C is the most prominent (1). Together with the negative volume of melting, it is responsible for the fact that water freezes from the top down and ice floats on water. The unusual behavior of water can be directly related to its ability to form hydrogen bonds (HBs) which are of strongly directional nature and determine the microscopic structure of water (2, 3). To investigate the anomalies of water at the molecular level, atomistic computer simulations have become an essential tool. Important contributions have been made by simulations using simple empirical water models (3–8).

Simulations based on ab initio molecular dynamics (AIMD) (9–11) allow determination of the properties of water with high predictive power and enable a detailed analysis of their underlying microscopic mechanisms. In contrast to empirical water models (5), which depend on experimental data resulting in a limited transferability, in AIMD the atomic forces that govern the molecular dynamics are obtained directly from quantum mechanics. Although this approach is in principle exact [in combination with methods that account for the quantum nature of the nuclei (12, 13)], ab initio simulations of condensed matter systems are feasible only if approximate but efficient methods such as density-functional theory (DFT) are used. Even then, however, simulations are restricted to short times and small systems. AIMD simulations have been used to a limited extent to investigate the phase behavior of water, for instance by estimating melting temperatures (14, 15) and vapor–liquid coexistence curves (16, 17). However, many fundamental thermodynamic properties of water have not been evaluated to date. To circumvent the limitations of on-the-fly AIMD, various efficient water potentials using data from ab initio calculations have been developed. For instance, existing water models have been reparametrized, based solely on forces from AIMD simulations (18) or using a combination of experimental and theoretical data (19). Other potentials use truncated many-body expansions of the water interaction energy, with parameters that are fitted to ab initio results for small water clusters (20–22). Recently, it was shown that a minimal water model with a coarse-grained electronic structure described by quantum Drude oscillators (23) (QDOs) is able to predict many thermodynamic properties of water (24).

Here, we present a series of analytic potentials which accurately represent the ab initio potential-energy surface of water and overcome the computational bottleneck of AIMD simulations, enabling assessment of the performance of different density functionals. The form of the potentials is not constructed using simplified physically motivated models, but instead consists of a set of highly flexible functions in the form of artificial neural networks (25, 26) trained to a broad range of condensed phase configurations. Using this powerful approach we carry out converged large-scale molecular dynamics simulations of water and clarify the significance of vdW interactions for the thermodynamic anomalies of water.

Results and Discussion

Neural Network Potentials. We developed four neural networks potentials (NNPs) representing the revised Perdew–Burke–Ernzerhof (RPBE) (27) and Becke–Lee–Yang–Parr (BLYP) (28, 29) density functionals with and without vdW corrections using the D3 method (30). Whereas NNPs can in principle be trained to any reference method, the majority of AIMD simulations for water reported to date have used gradient-corrected (GGA) DFT, and RPBE and BLYP are two well-established density functionals within this class.

The parameter set of each NNP was obtained in an iterative procedure using energies and forces from periodic configurations

Significance

Despite its simple chemical formula, H_2O, water is a complex substance with a variety of unusual properties resulting from its ability to form hydrogen bonds. A famous example for the anomalous behavior of water is the fact that it exhibits a density maximum at 4 °C. Here, we unravel the density anomaly of water on the molecular level using a powerful ab initio-based simulation technique. We show that weak van der Waals forces crucially modulate the flexibility of the hydrogen bond network, giving rise to the density maximum in water and causing ice to be less dense than the liquid.

Author contributions: T.M., C.D., and J.B. designed research; T.M. and A.S. performed research; T.M., A.S., C.D., and J.B. analyzed data; and T.M., A.S., C.D., and J.B. wrote the paper.

The authors declare no conflict of interest.

This article is a PNAS Direct Submission. C.J.M. is a guest editor invited by the Editorial Board.

Data deposition: The data reported in this manuscript are available at an online data repository, dx.doi.org/doi:10.6084/m9.figshare.1497907.

[1]To whom correspondence may be addressed. Email: tobias.morawietz@theochem.ruhr-uni-bochum.de or joerg.behler@theochem.ruhr-uni-bochum.de.

[2]Present address: Faculty of Physics, University of Vienna, A-1090 Vienna, Austria.

This article contains supporting information online at www.pnas.org/lookup/suppl/doi:10.1073/pnas.1602375113/-/DCSupplemental.

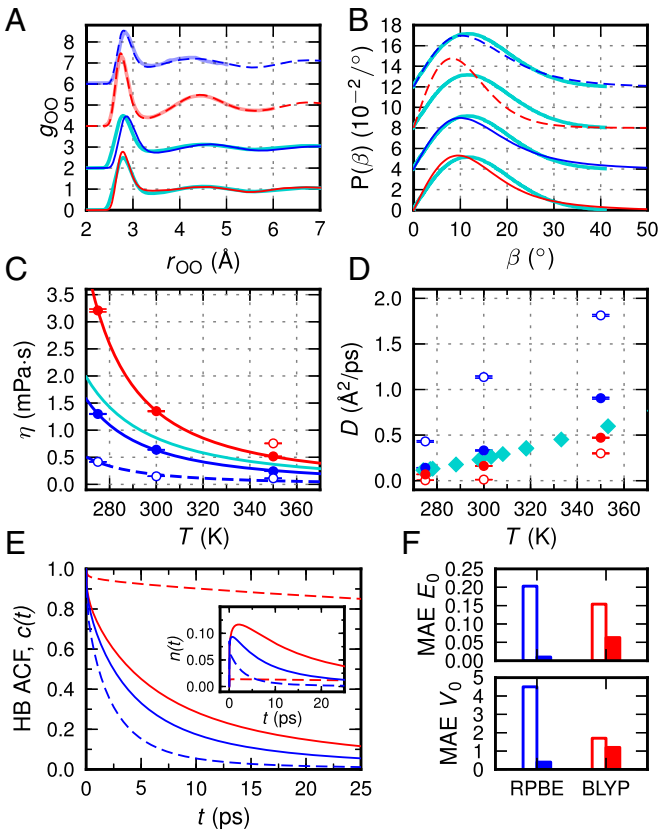

Fig. 1. Static and dynamic properties of liquid and crystalline water. (*A* and *B*) Structure of water at $T = 300$ K obtained from NNP simulations based on RPBE (dark-blue lines) and BLYP (dark-red lines) density functionals with (solid lines) and without (dashed lines) vdW corrections, compared with data from AIMD (12, 31) (light-blue and red lines) and experimental results (32, 33) (cyan lines). (*A*) Oxygen–oxygen radial distribution functions g_{OO} and (*B*) probability density function P(β) of the HB angle $\beta = \angle H_D - O_D \cdots O_A$. The curves are shifted for better visibility. (*C* and *D*) Viscosity η and diffusion coefficient *D* as function of temperature obtained from NNP simulations compared with experimental values (34, 35) (cyan line/cyan diamonds). Diffusion coefficients are corrected for finite size effects (compare *SI Appendix*, Fig. S4). Lines in *C* were obtained from a fit of the form: $\eta = (T - T_0)^{-b}$. (*E*) HB autocorrelation functions $c(t)$ and $n(t)$ (cf. ref. 36 and *SI Appendix*) obtained from NNP simulations at $T = 300$ K. (*F*) Mean absolute errors (MAEs) with respect to experiment of equilibrium lattice energies E_0 (in electronvolts per H_2O) and volumes V_0 (in cubic Ångstroms per H_2O) of seven ice phases computed at $T = 0$ K with NNPs based on plain (empty bars) and vdW-corrected (filled bars) density functionals. Energy vs. volume curves of all ice phases are reported in *SI Appendix*, Fig. S5.

of liquid and crystalline water under various conditions. Details concerning the functional form and the composition of the reference data set of the NNPs are given in *SI Appendix*. Root-mean-squared errors of energies and forces in the final NNP training sets are ≈ 2 meV/H_2 O and ≈ 70 meV/Å, respectively, and the error for configurations not included in the training set is of comparable order. Such errors are well below the intrinsic uncertainties of the DFT calculations related to the exchange–correlation functional and comparable to the much smaller error due to the finite basis set size. The NNPs closely reproduce the properties of liquid and crystalline water obtained from DFT calculations (compare Fig. 1*A* and *SI Appendix*, Figs. S3 and S5) and are thus well suited for assessing the quality of the underlying reference method. The inability of GGA density functionals to describe vdW forces can be compensated by vdW correction schemes (30). Comparing simulations with and without correction then allows us to investigate the effect of vdW interactions on the properties of water.

The large impact of vdW forces on the properties of liquid and crystalline water as obtained from NNP simulations is illustrated in Fig. 1. vdW interactions soften the water structure, reducing deviations from the experimental curves, and significantly improve lattice energies and volumes of various ice polymorphs. The influence on the dynamic properties depends on the respective density functional. Whereas the BLYP-based simulations exhibit very low water mobility, the opposite behavior is observed for RPBE. Including vdW interactions improves both methods, resulting in a more realistic description of the dynamics of water. Similar conclusions have been drawn from AIMD simulations (37–43) and static DFT calculations (44, 45). However, the specific influence of vdW interactions on the thermodynamic anomalies of water is still unclear. To understand the atomistic origin of these fundamental properties, we have carried out large-scale NNP simulations to determine the density isobar of water and the melting temperature of ice I*h*.

Density Isobars. Fig. 2*A* compares density isobars down to the supercooled regime obtained from constant pressure simulations at $P = 1$ bar to experimental data for bulk and confined water (46). Simulations without vdW corrections show poor agreement

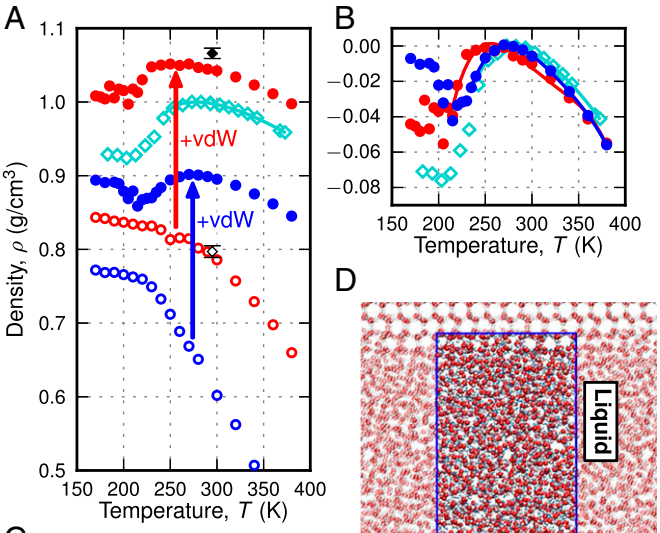

	T_m (K)	TMD (K)
BLYP	323 ± 3	—
BLYP-vdW	283 ± 2	256
RPBE	267 ± 2	—
RPBE-vdW	274 ± 3	274
Exp.	273.15	277.13

Fig. 2. Density isobars and melting temperature. (*A*) Density isobars at $P = 1$ bar obtained from NNP simulations based on the BLYP (red empty circles), BLYP-vdW (red filled circles), RPBE (blue empty circles), and RPBE-vdW (blue filled circles) density functionals. For comparison, experimental data for bulk (cyan line) and confined water (46) (cyan diamonds), and data from AIMD simulations with the vdW-corrected (black filled diamond) and uncorrected (black empty diamond) BLYP density functional (37) are also shown. (*B*) Densities relative to the density maximum. The density maxima for BLYP-vdW and RPBE-vdW were obtained from polynomial fits (red and blue lines) to the density isobars. (*C*) Melting temperature (T_m, errors were estimated by block averaging) and temperature of maximum density (TMD). Melting temperatures were corrected for deviations between the NNP and the DFT potential-energy surfaces (compare *SI Appendix*). (*D*) Snapshot of coexisting liquid water and ice I*h* taken from the interface pinning simulation used to determine the melting temperature (the simulation cell is drawn in blue).

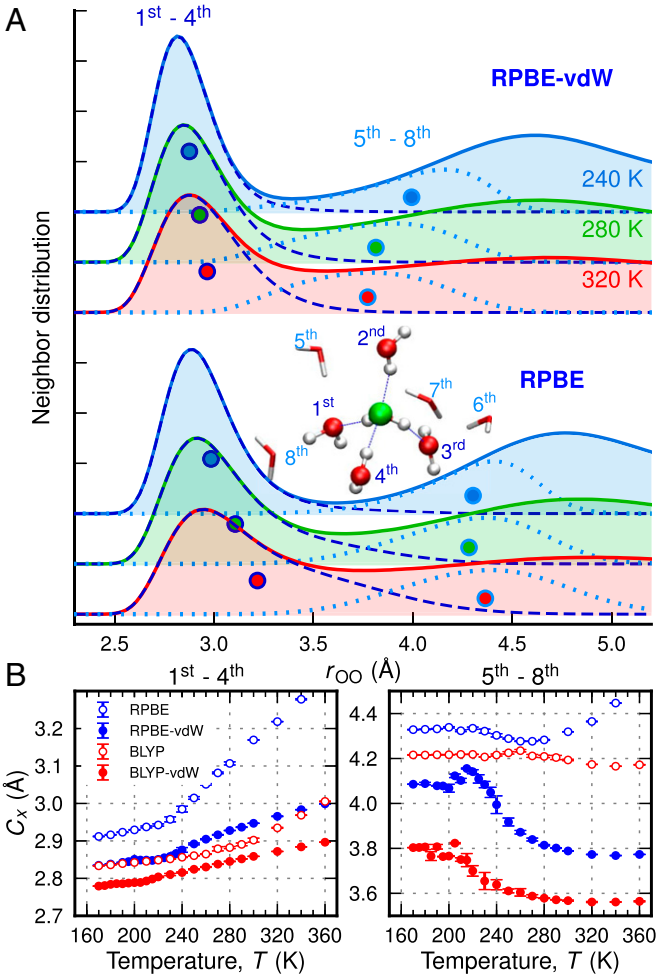

Fig. 3. Temperature dependence of water neighbor distribution. (*A*) Oxygen–oxygen radial distribution functions (solid lines) and decompositions into contributions from molecules in the first shell (first through fourth neighbors, dark-blue dashed lines) and part of the second shell (fifth through eighth neighbors, light-blue dotted lines) together with the centroid of the neighbor distribution (dark-blue and light-blue circles) for three different temperatures from simulations with (RPBE-vdW, *Top*) and without (RPBE, *Bottom*) vdW corrections. (*B*) Position of the neighbor distribution centroid C_x as function of temperature. In general, with decreasing temperature a contraction of the first shell is observed (*Left*), whereas only in vdW-corrected simulations a maximum of the total density is found due to the expansion of the second shell (*Right*).

with experiment: total densities are severely underestimated by 20–40%, no density maximum is observed, and the density increase upon cooling is too steep, resulting in strongly overestimated thermal expansivities at ambient conditions (compare *SI Appendix*, Table S4). In contrast, the inclusion of vdW forces leads to qualitatively correct results: both vdW-corrected potentials exhibit a density maximum, the shape of the isobars is in close agreement with experiment (compare Fig. 2*B*), and total densities are shifted to larger values [in agreement with AIMD simulations performed at a single state point (37, 39, 47)], reducing deviations from experiment to 5–10%. Moreover, a density minimum in the supercooled regime (at ≈ 200 K and ≈ 215 K for BLYP-vdW and RPBE-vdW, respectively) can be identified that is consistent with experimental measurements of water confined in silica pores (46) and simulations using empirical water models (7, 8). Comparable conclusions regarding the role of vdW forces in determining the density profile of water have been obtained from simulations with modified empirical water models: Truncating Lennard-Jones interactions resulted in reduced densities (15% lower compared with the full model) and the disappearance of the density maximum (48). Similar underestimated densities were found in simulations with the QDO water model, where the experimental value could be retained by increasing the strength of many-body dispersion (23).

Melting Temperatures. Exploiting the efficiency of NNPs, we have, for the first time to our knowledge, accurately computed the melting point of ice from first principles. Melting temperatures of ice I*h* obtained using the interface pinning method (49) are listed in Fig. 2*C*. Whereas the melting point is overestimated by about 50 K in BLYP-based simulations, all other potentials (based on BLYP-vdW, RPBE, and RPBE-vdW) agree within 10 K with experiment. However, only when vdW interactions are accounted for, liquid water is denser than ice at coexistence (compare *SI Appendix*, Table S5) and the anomalous melting behavior that causes water to freeze from the top down can be reproduced. Estimates of the melting temperature of water obtained earlier from AIMD simulations using the BLYP density functional have been reported to be 360 K with (14) and 411 K without (15) vdW corrections. Whereas the lowering of the melting point of about 50 K with inclusion of vdW forces is consistent with our results, the previous reported melting temperatures are much higher [for plain BLYP these high melting temperatures have been inconsistent with the calculated boiling point, which was estimated to be about 350 K (16)]. This discrepancy may be attributed to the limited system size (192 molecules) and simulation time (15 ps) of the AIMD simulations and the fact that they have been carried out at the experimental density of 1 g/cm^3 rather than at constant pressure. Whereas nuclear quantum effects (NQEs) not included here tend to weaken hydrogen bonds (50) and soften the structure of liquid water (12), they are unlikely to qualitatively change our findings for the thermodynamic properties of water. Melting temperatures are only weakly affected due to a competition between intra- and intermolecular NQEs (51–53). Further, simulations with ab initio-based potentials indicate that NQEs do not alter the location of the density maximum (54) and only marginally reduce the absolute water density (22, 54).

Water Neighbor Distribution. To identify the molecular origin of water's complex density isobar (exhibiting both a maximum and minimum) we have analyzed the structure of water by decomposing (55) the oxygen–oxygen radial distribution function into contributions from first- and second-shell molecules (Fig. 3). At high temperatures, thermal fluctuations weaken HBs and lead to an increased distance to hydrogen-bonded molecules in the first solvation shell. At the same time, second-shell molecules are able to penetrate the first shell [becoming interstitial molecules (43, 55, 56)] and perturb the local tetrahedral water network. Upon cooling, the HB strength increases and the first shell approaches the central molecule (Fig. 3*B*, *Left*), causing a density increase. However, this effect is compensated by a reduced number of interstitial molecules resulting in a shift of the second shell to larger distances, thus lowering the density (Fig. 3*B*, *Right*) and inducing a density maximum. Decreasing the temperature further, the expansion of the second shell finally saturates and the density increases again after passing through a minimum in the supercooled regime. Simulations without vdW corrections do not feature a pronounced second-shell shift, which explains the monotonic density increase with decreasing temperature in this case.

HB Analysis. The absence of the density maximum in the simulations without vdW corrections can be understood by examining the strength of the HB network. In Fig. 4 we analyze the fluctuations in the HB angle β, a measure of the HB strength, as a function of temperature. The different magnitudes of HB fluctuations indicate

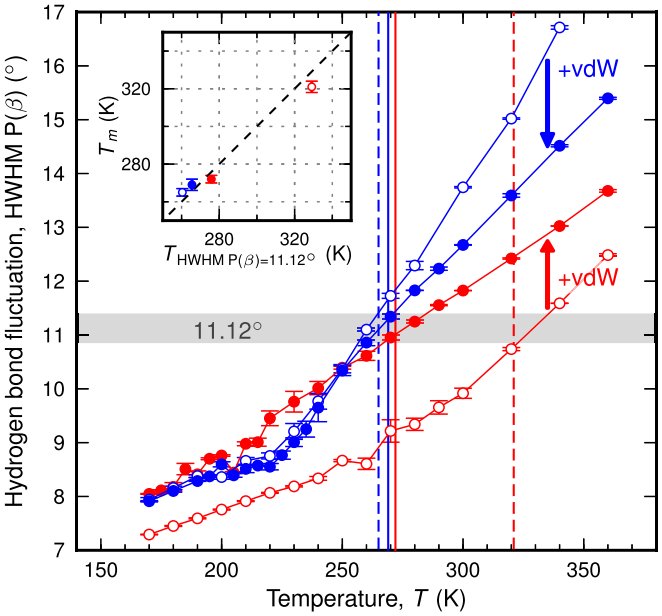

Fig. 4. HB fluctuation and melting temperature. Fluctuation in the HB angle β, measured by computing the half width at half maximum (HWHM) of the distribution function P(β), as a function of temperature obtained from NNP simulations based on the BLYP (red empty circles), BLYP-vdW (red filled circles), RPBE (blue empty circles), and RPBE-vdW (blue filled circles) density functionals. The vertical lines denote the melting temperature of the respective potentials (solid lines, vdW-corrected potentials; dashed lines, uncorrected potentials). (*Inset*) Correlation between melting temperature T_m and temperature of an HB fluctuation of 11.12°. The error bars of the melting temperatures were obtained by block averaging.

that HBs in uncorrected simulations are either too strong (BLYP) or too weak (RPBE) to yield a density maximum. In BLYP-based simulations the tetrahedral water network is too rigid, so that even in the high-temperature regime second-shell molecules are not able to penetrate the first solvation shell and a shift of the second shell at lower temperatures is prevented. HBs in RPBE-based simulations, on the other hand, are very weak, as manifested by large fluctuations in β and large distances of first-shell molecules, so that the first and second solvation shells are both shifted to smaller distances upon cooling until at ≈ 260 K HBs are strong enough to slightly reduce the number of interstitial molecules. This effect leads to a strong contraction of the system, resulting in high thermal expansivities (compare *SI Appendix*, Table S4) with an almost 10-fold increase over the experimental value. These results are in line with the observations made for the dynamic properties of water shown in Fig. 1 *C*–*E*.

Interestingly, we find that the HB fluctuations evaluated for the liquid phase can be used as a measure for the melting temperature of ice I*h*, T_m, in analogy to the Lindemann melting rule (57). For all NNPs used here, ice I*h* melts when the HB fluctuations exceed a critical value of ≈ 11° (compare Fig. 4), which explains the different values for T_m reported in Fig. 2*C*. To verify the correlation between HB strength and melting temperature, we performed simulations close to the melting temperature using a series of empirical water models. As shown in *SI Appendix*, Fig. S9, the critical fluctuation value at which melting occurs depends slightly on the class of water model. For models based on the 4-site transferable intermolecular potential (TIP4P) (5), a high degree of correlation is found at a critical value of ≈ 10°.

The fact that vdW corrections either weaken (BLYP) or strengthen (RPBE) HBs is related to the vdW correction terms which are different for the two density functionals (*SI Appendix*, Table S7). For RPBE, the vdW interactions between pairs of oxygen and hydrogen atoms (Fig. 5*B*, *Left*) have a deep minimum at short OH distances increasing the HB strength by reducing the probability of configurations with extended intermolecular OH distances (compare Fig. 5*A*, *Left*). In contrast, the BLYP vdW pair interaction (Fig. 5*B*, *Right*) is weaker and shifted to larger distances, inducing an increased population of extended HBs with reduced strength (Fig. 5*A*, *Right*). Similar observations can be made for vdW interactions between pairs of oxygen atoms, shown in *SI Appendix*, Fig. S10. Both effects are clearly visible in the probability density functions of HB angle and OH distance (Fig. 5*C*): HBs are very flexible in the case of RPBE and very stiff in the case of BLYP. Both vdW-corrected density functionals show similar distributions in between the uncorrected probability density functions.

Dielectric Properties. We conclude by analyzing the influence of vdW interactions on the dielectric properties of liquid water. Calculating the dielectric constant from molecular dynamics (MD) simulations requires simulation times of several nanoseconds. Whereas rough estimates based on short AIMD trajectories have been made (58, 59), converged values have not been obtained to date. We have computed converged dielectric constants at 300 K by generating independent configurations in NNP simulations, which we then used to calculate molecular dipole moments from maximally localized Wannier functions (60) (*SI Appendix*). Whereas the dielectric constant is overestimated in simulations without vdW interactions (159.8 and 108.9 for BLYP and RPBE, respectively) compared with the experimental value of 78.4, the values improve if vdW forces are accounted for (106.2 and 95.2 for BLYP-vdW and RPBE-vdW, respectively) which is associated

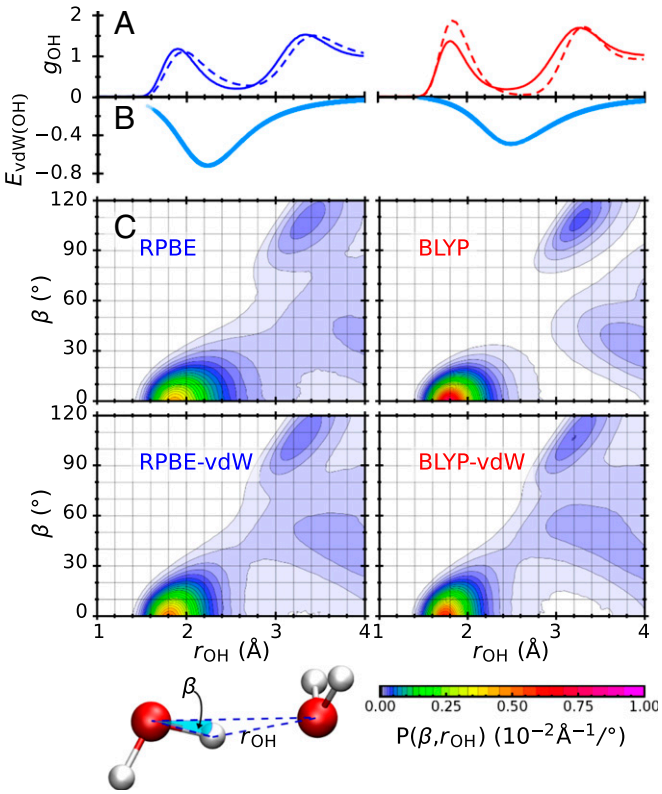

Fig. 5. Effect of vdW interactions on HB geometry. (*A*) Intermolecular oxygen–hydrogen radial distribution functions g_{OH} from NNP simulations at 300 K based on the RPBE (*Left*) and BLYP (*Right*) density functionals with (solid lines) and without (dashed lines) vdW corrections. (*B*) vdW pair interaction energy $E_{vdW(OH)}$ (in units of k_BT, where k_BT is Boltzmann's constant times temperature) between oxygen and hydrogen atoms as a functions of the pair distance r_{OH} obtained from the NNP simulations. (*C*) Probability density function P(β,r_{OH}) of the HB angle β and the oxygen–hydrogen distance r_{OH}.

with a shift of the molecular dipole moment distributions to lower values (*SI Appendix*, Fig. S6*A*) in agreement with results from AIMD simulations (43).

Conclusions

In summary, we have shown that ab initio-based NNP simulations are able to correctly predict water's density maximum and melting temperature provided that vdW forces are taken into account, highlighting the important role of these interactions in determining the properties of aqueous systems. Despite their rather weak and anisotropic nature, vdW forces crucially modulate the HB network and ensure the right level of flexibility that causes the anomalous behavior of water. These results demonstrate the predictive power of AIMD simulations compared with empirical water models [whose density maximum is usually underestimated if experimental density information is not explicitly included in the parametrization process (61)]. They further indicate that liquid water and ice can be accurately described already on the GGA level of theory if vdW corrections are considered without the need to include exact exchange in the form of computationally demanding hybrid density functionals. NNP simulations of water are thus a reliable and predictive tool which could also help investigate other important properties such as the existence of a liquid–liquid transition in water at supercooled conditions (4, 6). Unlike most water models, NNPs are capable of describing the making and breaking of chemical bonds, opening the possibility to study proton transfer and autoionization in the condensed phase.

Methods

MD simulations were performed with an extended version of the LAMMPS program (62) using four ab initio-based NNPs for water representing RPBE (27) and BLYP (28, 29) density functionals with and without vdW corrections using the D3 method (30). Parameter sets for all NNPs are publicly available (dx.doi.org/doi:10.6084/m9.figshare.1497907).

Distribution functions compared with previous AIMD results (Fig. 1*A*, top two curves) were computed in the canonical (*NVT*) ensemble at a density of 1 g/cm^3, whereas for a comparison with experiment (Fig. 1*A*, bottom two curves and Fig. 1*B*) simulations were run in the isothermal–isobaric (*NPT*) ensemble (see below). Dynamic properties (Fig. 1 *C*–*E*) were obtained in the following way: For each NNP and temperature the equilibrium volume was determined by *NPT* simulations as described below. Then, simulations in the *NVT* ensemble were carried out for 1 ns using 512 water molecules and a time step of 0.5 fs. Thirty-two statistically independent sets of coordinates and velocities were extracted from each *NVT* trajectory and used as starting points for simulations in the microcanonical (*NVE*) ensemble with a simulation time of 200 ps per trajectory. After discarding the first 50 ps for the purpose of equilibration, viscosities and diffusion coefficients corrected for finite size effects were determined (see *SI Appendix* for details). HB kinetics were analyzed in terms of the Luzar–Chandler model (36) and computed with the GROMACS package (63, 64). The vibrational density of states (VDOS) spectrum shown in *SI Appendix*, Fig. S3 was computed from velocity autocorrelation functions obtained from 16 independent *NVE* simulations with a length of 20 ps using initial configurations from an *NVT* trajectory at 300 K.

Density isobars at 1 bar covering a temperature range from 380 to 170 K in steps of 5–20 K were obtained from MD simulations of 128 water molecules in the *NPT* ensemble with a time step of 0.5 fs and using the equations of motion of Shinoda et al. (65). As shown in *SI Appendix*, Fig. S7, simulation cells containing 128 molecules are sufficient to obtain converged density isobars. The simulation length at each single temperature was 2–20 ns (depending on temperature and convergence behavior), resulting in a total simulation time of more than 700 ns. Configurations from equilibrated simulations in the *NVT* ensemble were used as starting points for the *NPT* simulations at 380 K. Subsequently, simulations at lower temperatures were performed step by step by using the final configuration of the preceding simulation as initial configuration. The first halves of the trajectories served for equilibration and were not used for analyses. Density maxima and thermal expansivities at $T = 25$ °C were obtained from polynomial fits (fourth order for BLYP-vdW and RPBE-vdW, third order for BLYP and RPBE) to the density isobars.

Melting temperatures of ice I*h* were computed using the interface pinning method (49, 66) (see *SI Appendix* for details). The densities of the liquid and the solid phase reported in *SI Appendix*, Table S5 were obtained from separate *NPT* simulations carried out at T_m using 2,304 water molecules and simulation times of 1 ns (after equilibrating for 0.5 ns). To account for possible differences between the DFT and the NNP potential-energy surfaces, the melting temperatures were corrected using thermodynamic perturbation theory as described in *SI Appendix*. All correction terms have positive values which range from 2 to 11 K (*SI Appendix*, Table S6).

ACKNOWLEDGMENTS. The authors thank S. Imoto, H. Forbert, D. Marx, and M. Heyden for insightful discussions and providing AIMD data; and A. Urban and N. Artrith for help with the Vienna ab initio simulation package (VASP) and Wannier90. The results presented here have been achieved in part using the Vienna Scientific Cluster (VSC). This work was supported by the Cluster of Excellence RESOLV (Ruhr Explores Solvation: EXC 1069) funded by the Deutsche Forschungsgemeinschaft (DFG), as well as by the DFG Emmy Noether Project Be3264/3-1, Heisenberg Fellowship Be3264/6-1, and Project Be3264/5-1. T.M. is grateful for a PhD Fellowship of the Studienstiftung des Deutschen Volkes and for support by the Ruhr-University Research School Plus (DFG GSC 98/3). A.S. is grateful for support by the VSC Research Center funded by the Austrian Federal Ministry of Science, Research and Economy (bmwfw). Financial support of the Austrian Science Fund (FWF) (Projects P24681-N20 and SFB Vicom, F41) is gratefully acknowledged.

1. Ludwig R (2001) Water: From clusters to the bulk. *Angew Chem Int Ed Engl* 40(10): 1808–1827.
2. Stillinger FH (1980) Water revisited. *Science* 209(4455):451–457.
3. Mishima O, Stanley HE (1998) The relationship between liquid, supercooled and glassy water. *Nature* 396(6709):329–335.
4. Palmer JC, et al. (2014) Metastable liquid-liquid transition in a molecular model of water. *Nature* 510(7505):385–388.
5. Jorgensen WL, Chandrasekhar J, Madura JD, Impey RW, Klein ML (1983) Comparison of simple potential functions for simulating liquid water. *J Chem Phys* 79(2):926–935.
6. Poole PH, Sciortino F, Essmann U, Stanley HE (1992) Phase-behavior of metastable water. *Nature* 360(6402):324–328.
7. Paschek D (2005) How the liquid-liquid transition affects hydrophobic hydration in deeply supercooled water. *Phys Rev Lett* 94(21):217802.
8. Poole PH, Saika-Voivod I, Sciortino F (2005) Density minimum and liquid-liquid phase transition. *J Phys Condens Matter* 17(43):L431–L437.
9. Car R, Parrinello M (1985) Unified approach for molecular dynamics and density-functional theory. *Phys Rev Lett* 55(22):2471–2474.
10. Marx D, Hutter J (2009) *Ab Initio Molecular Dynamics: Basic Theory and Advanced Methods* (Cambridge Univ Press, Cambridge, UK).
11. Hassanali AA, Cuny J, Verdolino V, Parrinello M (2014) Aqueous solutions: State of the art in ab initio molecular dynamics. *Philos Trans A Math Phys Eng Sci* 372(2011):20120482.
12. Morrone JA, Car R (2008) Nuclear quantum effects in water. *Phys Rev Lett* 101(1):017801.
13. Ceriotti M, Cuny J, Parrinello M, Manolopoulos DE (2013) Nuclear quantum effects and hydrogen bond fluctuations in water. *Proc Natl Acad Sci USA* 110(39):15591–15596.
14. Yoo S, Zeng XC, Xantheas SS (2009) On the phase diagram of water with density functional theory potentials: The melting temperature of ice I(h) with the Perdew-Burke-Ernzerhof and Becke-Lee-Yang-Parr functionals. *J Chem Phys* 130(22):221102.
15. Yoo S, Xantheas SS (2011) Communication: The effect of dispersion corrections on the melting temperature of liquid water. *J Chem Phys* 134(12):121105.
16. McGrath MJ, et al. (2006) Simulating fluid-phase equilibria of water from first principles. *J Phys Chem A* 110(2):640–646.
17. McGrath MJ, Siepmann JI, Kuo IFW, Mundy CJ (2006) Vapor-liquid equilibria of water from first principles: Comparison of density functionals and basis sets. *Mol Phys* 104(22-24): 3619–3626.
18. Spura T, John C, Habershon S, Kühne TD (2015) Nuclear quantum effects in liquid water from path-integral simulations using an ab initio force matching approach. *Mol Phys* 113(8):808.
19. Wang LP, Martinez TJ, Pande VS (2014) Building force fields: An automatic, systematic, and reproducible approach. *J Phys Chem Lett* 5(11):1885–1891.
20. Wang YM, Bowman JM (2010) Towards an ab initio flexible potential for water, and post-harmonic quantum vibrational analysis of water clusters. *Chem Phys Lett* 491(1-3):1–10.
21. Bartok AP, Gillan MJ, Manby FR, Csanyi G (2013) Machine-learning approach for one- and two-body corrections to density functional theory: Application to molecular and condensed water. *Phys Rev B* 88(5):054104.
22. Medders GR, Babin V, Paesani F (2014) Development of a "first-principles" water potential with flexible monomers. III. Liquid phase properties. *J Chem Theory Comput* 10(8):2906–2910.
23. Jones A, Cipcigan F, Sokhan VP, Crain J, Martyna GJ (2013) Electronically coarse-grained model for water. *Phys Rev Lett* 110(22):227801.
24. Sokhan VP, Jones AP, Cipcigan FS, Crain J, Martyna GJ (2015) Signature properties of water: Their molecular electronic origins. *Proc Natl Acad Sci USA* 112(20):6341–6346.
25. Behler J, Parrinello M (2007) Generalized neural-network representation of high-dimensional potential-energy surfaces. *Phys Rev Lett* 98(14):146401.
26. Behler J (2014) Representing potential energy surfaces by high-dimensional neural network potentials. *J Phys Condens Matter* 26(18):183001.
27. Hammer B, Hansen LB, Norskov JK (1999) Improved adsorption energetics within density-functional theory using revised Perdew-Burke-Ernzerhof functionals. *Phys Rev B* 59(11):7413–7421.

28. Becke AD (1988) Density-functional exchange-energy approximation with correct asymptotic behavior. *Phys Rev A Gen Phys* 38(6):3098–3100.
29. Lee C, Yang W, Parr RG (1988) Development of the Colle-Salvetti correlation-energy formula into a functional of the electron density. *Phys Rev B Condens Matter* 37(2): 785–789.
30. Grimme S, Antony J, Ehrlich S, Krieg H (2010) A consistent and accurate ab initio parametrization of density functional dispersion correction (DFT-D) for the 94 elements H-Pu. *J Chem Phys* 132(15):154104.
31. Fernandez-Serra MV, Ferlat G, Artacho E (2005) Two exchange-correlation functionals compared for first-principles liquid water. *Mol Simul* 31(5):361–366.
32. Soper AK (2013) The radial distribution functions of water as derived from radiation total scattering experiments: Is there anything we can say for sure? *ISRN Phys Chem* 2013:279463.
33. Modig K, Pfrommer BG, Halle B (2003) Temperature-dependent hydrogen-bond geometry in liquid water. *Phys Rev Lett* 90(7):075502.
34. Yoshida K, Wakai C, Matubayasi N, Nakahara M (2005) A new high-temperature multinuclear-magnetic-resonance probe and the self-diffusion of light and heavy water in sub- and supercritical conditions. *J Chem Phys* 123(16):164506.
35. Bird R, Stewart W, Lightfoot E (2002) *Transport Phenomena* (Wiley, New York), 2nd Ed.
36. Luzar A, Chandler D (1996) Hydrogen-bond kinetics in liquid water. *Nature* 379(6560):55–57.
37. Del Ben M, Hutter J, VandeVondele J (2015) Probing the structural and dynamical properties of liquid water with models including non-local electron correlation. *J Chem Phys* 143(5):054506.
38. Lin IC, Seitsonen AP, Coutinho-Neto MD, Tavernelli I, Rothlisberger U (2009) Importance of van der Waals interactions in liquid water. *J Phys Chem B* 113(4):1127–1131.
39. Schmidt J, et al. (2009) Isobaric-isothermal molecular dynamics simulations utilizing density functional theory: An assessment of the structure and density of water at near-ambient conditions. *J Phys Chem B* 113(35):11959–11964.
40. Wang J, Román-Pérez G, Soler JM, Artacho E, Fernández-Serra MV (2011) Density, structure, and dynamics of water: The effect of van der Waals interactions. *J Chem Phys* 134(2):024516.
41. Ma Z, Zhang Y, Tuckerman ME (2012) Ab initio molecular dynamics study of water at constant pressure using converged basis sets and empirical dispersion corrections. *J Chem Phys* 137(4):044506.
42. Forster-Tonigold K, Groß A (2014) Dispersion corrected RPBE studies of liquid water. *J Chem Phys* 141(6):064501.
43. DiStasio RA, Jr, Santra B, Li Z, Wu X, Car R (2014) The individual and collective effects of exact exchange and dispersion interactions on the ab initio structure of liquid water. *J Chem Phys* 141(8):084502.
44. Santra B, et al. (2011) Hydrogen bonds and van der Waals forces in ice at ambient and high pressures. *Phys Rev Lett* 107(18):185701.
45. Brandenburg JG, Maas T, Grimme S (2015) Benchmarking DFT and semiempirical methods on structures and lattice energies for ten ice polymorphs. *J Chem Phys* 142(12):124104.
46. Mallamace F, et al. (2007) The anomalous behavior of the density of water in the range 30 K < T < 373 K. *Proc Natl Acad Sci USA* 104(47):18387–18391.
47. Gaiduk AP, Gygi F, Galli G (2015) Density and compressibility of liquid water and ice from first-principles simulations with hybrid functionals. *J Phys Chem Lett* 6(15): 2902–2908.
48. Remsing RC, Rodgers JM, Weeks JD (2011) Deconstructing classical water models at interfaces and in bulk. *J Stat Phys* 145(2):313–334.
49. Pedersen UR, Hummel F, Kresse G, Kahl G, Dellago C (2013) Computing Gibbs free energy differences by interface pinning. *Phys Rev B* 88(9):094101.
50. Soper AK, Benmore CJ (2008) Quantum differences between heavy and light water. *Phys Rev Lett* 101(6):065502.
51. Habershon S, Markland TE, Manolopoulos DE (2009) Competing quantum effects in the dynamics of a flexible water model. *J Chem Phys* 131(2):024501.
52. Markland TE, Berne BJ (2012) Unraveling quantum mechanical effects in water using isotopic fractionation. *Proc Natl Acad Sci USA* 109(21):7988–7991.
53. Romanelli G, et al. (2013) Direct measurement of competing quantum effects on the kinetic energy of heavy water upon melting. *J Phys Chem Lett* 4(19):3251–3256.
54. Paesani F, Iuchi S, Voth GA (2007) Quantum effects in liquid water from an ab initio-based polarizable force field. *J Chem Phys* 127(7):074506.
55. Saitta AM, Datchi F (2003) Structure and phase diagram of high-density water: The role of interstitial molecules. *Phys Rev E Stat Nonlin Soft Matter Phys* 67(2 Pt 1): 020201.
56. Jedlovszky P, Mezei M, Vallauri R (2000) A molecular level explanation of the density maximum of liquid water from computer simulations with a polarizable potential model. *Chem Phys Lett* 318(1-3):155–160.
57. Lindemann FA (1910) Über die Berechnung molekularer Eigenfrequenzen. *Phys Z* 11: 609–612.
58. Silvestrelli PL, Parrinello M (1999) Structural, electronic, and bonding properties of liquid water from first principles. *J Chem Phys* 111(8):3572–3580.
59. Sharma M, Resta R, Car R (2007) Dipolar correlations and the dielectric permittivity of water. *Phys Rev Lett* 98(24):247401.
60. Marzari N, Vanderbilt D (1997) Maximally localized generalized Wannier functions for composite energy bands. *Phys Rev B* 56(20):12847–12865.
61. Vega C, Abascal JLF (2005) Relation between the melting temperature and the temperature of maximum density for the most common models of water. *J Chem Phys* 123(14):144504.
62. Plimpton S (1995) Fast parallel algorithms for short-range molecular dynamics. *J Comput Phys* 117(1):1–19.
63. Van Der Spoel D, et al. (2005) GROMACS: Fast, flexible, and free. *J Comput Chem* 26(16):1701–1718.
64. van der Spoel D, van Maaren PJ, Larsson P, Tîmneanu N (2006) Thermodynamics of hydrogen bonding in hydrophilic and hydrophobic media. *J Phys Chem B* 110(9): 4393–4398.
65. Shinoda W, Shiga M, Mikami M (2004) Rapid estimation of elastic constants by molecular dynamics simulation under constant stress. *Phys Rev B* 69(13):134103.
66. Pedersen UR (2013) Direct calculation of the solid-liquid Gibbs free energy difference in a single equilibrium simulation. *J Chem Phys* 139(10):104102.